ENGINEERING

Sustained drag reduction in a turbulent flow using a low-temperature Leidenfrost surface

Dhananjai Saranadhi,[1]* Dayong Chen,[2]* Justin A. Kleingartner,[2] Siddarth Srinivasan,[2,3] Robert E. Cohen,[2†] Gareth H. McKinley[1†]

Skin friction drag contributes a major portion of the total drag for small and large water vehicles at high Reynolds number (Re). One emerging approach to reducing drag is to use superhydrophobic surfaces to promote slip boundary conditions. However, the air layer or "plastron" trapped on submerged superhydrophobic surfaces often diminishes quickly under hydrostatic pressure and/or turbulent pressure fluctuations. We use active heating on a superhydrophobic surface to establish a stable vapor layer or "Leidenfrost" state at a relatively low superheat temperature. The continuous film of water vapor lubricates the interface, and the resulting slip boundary condition leads to skin friction drag reduction on the inner rotor of a custom Taylor-Couette apparatus. We find that skin friction can be reduced by 80 to 90% relative to an unheated superhydrophobic surface for Re in the range $26,100 \leq Re \leq 52,000$. We derive a boundary layer and slip theory to describe the hydrodynamics in the system and show that the plastron thickness is $h = 44 \pm 11\ \mu m$, in agreement with expectations for a Leidenfrost surface.

INTRODUCTION

Hydrodynamic drag resulting from the action of fluid viscosity not only results in large power requirements for water vehicles but also imposes an upper bound on vehicle speed. Extensive research efforts have been focused on drag reduction, and a variety of strategies have been developed, including fabrication of specific surface topographic features (1, 2), injection of viscoelastic polymer additives near the surface (3, 4), establishing a slip condition (5–13), and, most recently, phase transition at the solid/liquid interface (14). In turbulent flows, the nonslip boundary condition at a solid/liquid interface results in skin friction drag that contributes to 60 to 70% of the total drag for large cargo ships and 90% for underwater vehicles (15), depending on the Reynolds number (Re) ($Re = \rho VL/\mu$, characterizing the flow past the object). Numerous studies have sought to reduce skin friction drag by locally surrounding the immersed solid boundary with another low-viscosity fluid, creating an effective slip boundary condition (5–12, 16). The low viscosity of gases relative to that of liquids (typically on the order of $10^{-3} \leq \mu_v/\mu_l \leq 10^{-2}$) makes them ideal candidates to serve as local lubricating fluids for promoting drag reduction (8, 15). This gas film can be created by submerging a textured superhydrophobic surface from air into water, leading to the trapping of microscopic gas packets in the surface texture, forming a Cassie-Baxter state (17, 18). The resulting partial slip boundary condition gives rise to a nonzero average value of the slip length $\bar{b} = V_{slip}\mu_l/\bar{\tau}_w$ (where V_{slip} is the slip speed at the wall and $\bar{\tau}_w$ is the average wall shear stress), leading to modest skin friction reduction typically in the range of 5 to 25% (7, 19–22). These levels of frictional drag reduction equate to reductions in fuel costs of 15 to 40%, depending on the water vehicle speed and its hull form. However, for a submerged superhydrophobic surface, the plastron is typically meta-stable; diffusion and pressure fluctuations tend to gradually deplete the gas layer, leading to the progressive loss of drag reduction over time (23–26).

To maintain a persistent lubricating gas layer, active delivery to (or generation of gas at) the solid/liquid interface is required (15, 27). One attractive approach is to create a lubricating vapor layer through film boiling, using waste heat generated from the power plant of an oceangoing vessel that can be redistributed across the wetted surface (28). Typical pool boiling curves for water on different surfaces are illustrated in Fig. 1A. Initially, the heat flux increases as the intensity of nucleate boiling increases with the wall superheat ($\Delta T = T_W - T_{sat}$) until it reaches a local maximum—the critical heat flux (CHF). A further increase in superheat then leads to a decrease in heat flux as a continuous vapor film begins to form on the surface. The film reaches its maximum width and completely encompasses the body at the Leidenfrost temperature (T_L) (29–31). The region to the right of this point is known as the film boiling regime and is the ideal operating regime for establishing a skin friction–reducing film or plastron. A recent example demonstrated that establishing a vapor film around a submerged sphere by initially superheating the body past its Leidenfrost temperature leads to significant drag reduction (9, 16). However, this transient observation only persisted over a short period of time before heat transfer across the film resulted in the sphere being cooled to below Leidenfrost temperature, and then the boiling film collapses back into the nucleate boiling regime, with a concomitant increase in frictional drag.

Creating a sustained boiling film requires substantial power input, depending on the roughness and wettability of the surfaces (32–34). The values of CHF and T_L for metals, such as smooth aluminum, are approximately CHF $\approx$ 500 kW/m^2 and $T_L \approx$ 270°C (35). However, using textured superhydrophobic surfaces can substantially reduce these values (32, 34). The lowered surface energy and three-dimensional (3D) texture result in an energetically favorable Cassie-Baxter state (36). Limited heat transfer occurs through the small areas of contact between the surface topography and the wetting liquid. Therefore, heating the surface results in a rapid transition to film boiling with no or little nucleation taking place (34). Here, we take advantage of the low-temperature Leidenfrost characteristic of a superhydrophobic surface to minimize the power input required to sustain a lubricating vapor film on the surface of a rotating cylinder immersed in a liquid in a Taylor-Couette cell. We show that active heating leads to 80 to 90% drag reduction with respect to the unheated state. From our measurement of the torque/velocity relationship and an appropriate model for the boundary condition at the

[1]Department of Mechanical Engineering, Massachusetts Institute of Technology, Cambridge, MA 02139, USA. [2]Department of Chemical Engineering, Massachusetts Institute of Technology, Cambridge, MA 02139, USA. [3]School of Engineering and Applied Sciences, Harvard University, Cambridge, MA 02138, USA.
*These authors contributed equally to this work.
†Corresponding author. Email: recohen@mit.edu (R.E.C.); gareth@mit.edu (G.H.M.)
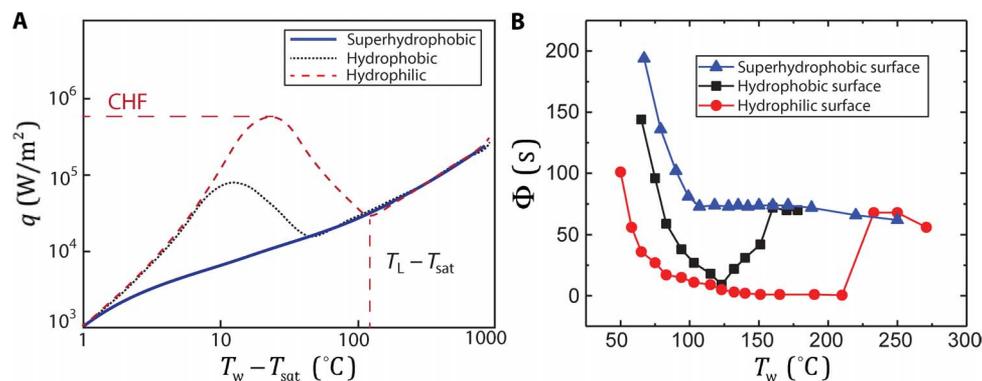
Fig. 1. (A) A schematic of pool boiling curves on three surfaces with different physicochemical properties: a smooth hydrophilic surface (red dashed), a smooth hydrophobic surface (black dotted), and a textured superhydrophobic surface (blue solid). As the superheat [$\Delta T = T_w - T_{sat}$, defined as the wall temperature (T_w) minus the saturated water boiling temperature] increases, the heat flux (q) increases until it reaches a local maximum (CHF), followed by decreasing to a local minimum corresponding to the Leidenfrost temperature (T_L), before increasing again. Compared to a smooth hydrophilic surface, a suitably textured superhydrophobic surface can smoothly transition to a Leidenfrost state without a CHF. **(B)** We determine the Leidenfrost transition by measuring the lifetime of a droplet (with an initial volume of 10 μl). As the wall temperature increases, the lifetime (Φ) decreases rapidly until it reaches a minimum and then rapidly increases to a local maximum (corresponding to T_L) as the vapor film of the Leidenfrost state is fully established. The measured droplet lifetime at $T_w = 125$°C increases from ~5 s on the smooth hydrophilic or smooth hydrophobic surfaces to approximately 75 s on the superhydrophobic textured surface.

surface of the turbulent flow, we extract a slip length of $b = 1.04 \pm 0.26$ mm.

RESULTS AND DISCUSSION

Using superhydrophobic surfaces substantially lowers the heat flux to establish the Leidenfrost state (*34*). This marked change in local boiling condition can be quantified by tracking the evaporation rate of a droplet as a function of surface temperature (*35*). As shown in Fig. 1B, we characterize T_L by measuring the lifetime of a droplet as a function of surface temperature for three surfaces with different physicochemical properties. As the surface temperature of a smooth untreated silicon substrate increases, the lifetime decreases rapidly until it reaches a minimum and then rapidly increases to a local maximum followed by another slow decrease. The local maximum in the droplet lifetime corresponds to T_L, where the heat flux is at its local minimum [Fig. 1A shows a schematic of pool boiling curves for three different types of surfaces; quantitative measurements of the boiling curves for these surfaces have recently been reported by Fan *et al.* (*34*); see also the Supplementary Materials in Vakarelski *et al.* (*33*)]. A smooth hydrophilic surface (for example, bare silicon wafer with a water-advancing contact angle of $\theta_{adv} = 34 \pm 2$° and a water-receding contact angle of $\theta_{rec} = 0$°) is determined to have $T_L = 230$°C, whereas a smooth hydrophobic surface (silicon wafer functionalized with perfluorooctyltriethoxysilane, $\theta_{adv} = 121 \pm 1$° and $\theta_{rec} = 89 \pm 2$°) lowers the Leidenfrost temperature to $T_L = 160$°C. A properly treated metallic superhydrophobic surface (for preparation details, see Materials and Methods) can smoothly transition to a Leidenfrost surface without any clear indication of a CHF (*33*). However, other published experimental results suggest that a small minimum in the droplet lifetime (corresponding to a CHF) may persist for other types of superhydrophobic surfaces (*32, 34, 37*), albeit with large experimental uncertainty. This picture is consistent with our observations, shown in Fig. 1B, for the temperature dependence of the lifetime of a drop on a superhydrophobic surface. The data show a shallow but reproducible minimum, consistent with a small CHF. The smoothness and monotonicity of this transition will depend on three-

phase contact line pinning events beneath the boiling droplet and other local features of the surface topography, and further research is required to resolve the precise details of the transition. As shown in Fig. 2A, the water-advancing and water-receding contact angles on this superhydrophobic surface are $\theta_{adv} = 161 \pm 1$° and $\theta_{rec} = 160 \pm 1$°, respectively. In Fig. 2B, two superhydrophobic cylindrical Couette rotors (used in the subsequent drag reduction experiments) with identical dimensions are immersed in water. The rotor on the right is kept at room temperature and appears dark owing to a partially wetted boundary, whereas the rotor on the left is superheated to 125°C, leading to a continuous vapor film, which appears as a silvery plastron.

We prepare such a superhydrophobic surface by creating controlled microstructures through etching 6061 aluminum in a solution of 18 weight % (wt%) hydrochloric acid for 90 s, followed by passivation in a furnace at 600°C for 24 hours, which helps to reduce the rate of boehmitization of the metal in boiling water in the later experiments (*38*). The textured metal is rendered superhydrophobic by immersing it in a solution of perfluorooctyltriethoxysilane and hexane (7 μl/ml) for 24 hours, followed by baking it in an oven at 120°C for 1 hour to ensure covalent chemical bonding of silane molecules to the surface. Although a number of different methods for preparing superhydrophobic surfaces exist, one advantage of this approach is that it can treat metal objects of arbitrary shape, such as Taylor-Couette rotors that can be used in standard rheometers to quantify the torque-speed relationship. Moreover, in contrast to the spray-on polymer-based surface textures we have used previously (*7*), which tend to anneal and smooth above their glass transition temperatures, the texture on the etched aluminum surface and the chemically attached silane molecules can be stable up to 300°C, which is ideal for high-temperature applications. These advantages allow for the repeatable and high-precision fabrication of a cylindrical Taylor-Couette rotor with a uniform and thermally stable superhydrophobic surface. Figure 2 (C and D) shows a scanning electron micrograph and an atomic force micrograph of the superhydrophobic surface, respectively. The former highlights the randomly rough texture uniformly distributed over a large area, whereas the latter shows the local 3D profile of the superhydrophobic surface texture, from which the
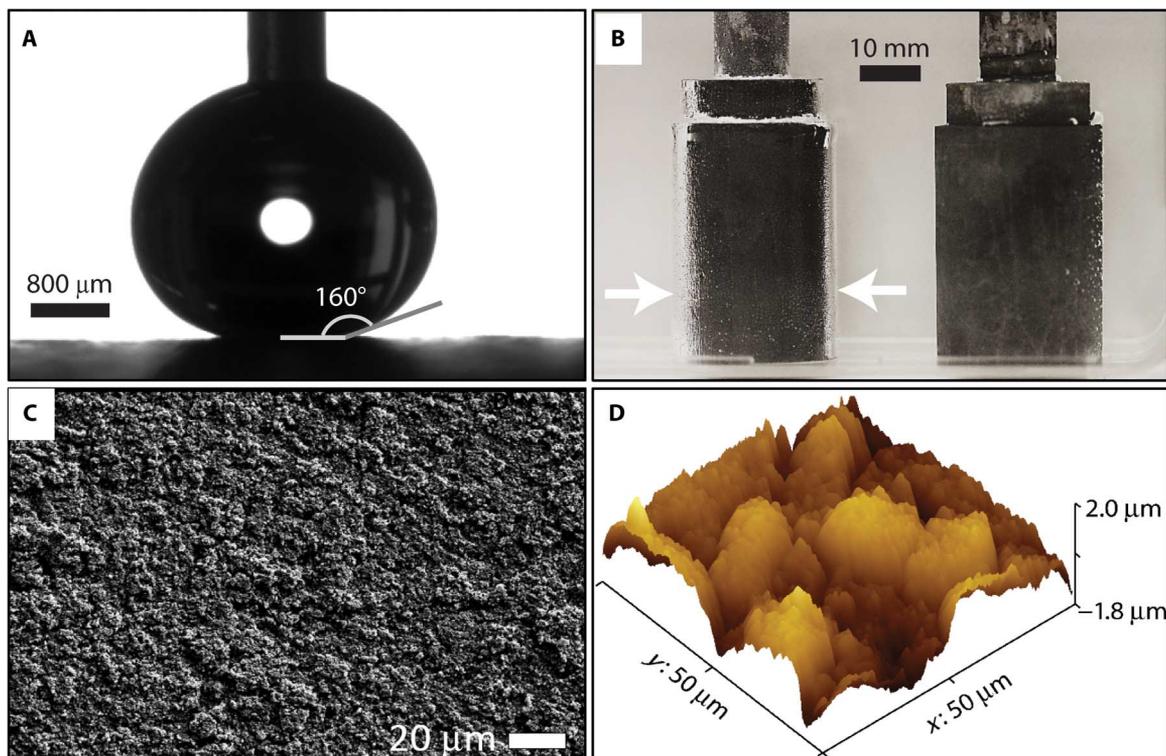
Fig. 2. A low-temperature Leidenfrost superhydrophobic surface. (**A**) A water droplet on the superhydrophobic surface, exhibiting a contact angle of θ = 160°. (**B**) Two identical superhydrophobic rotors immersed in water. The rotor on the left is at 125°C, showing a thick, continuous vapor film. The rotor on the right is at room temperature and consequently has no observable vapor film. (**C**) A scanning electron micrograph of the superhydrophobic surface. (**D**) An atomic force micrograph showing the 3D profile of the same surface. The surface roughness parameters calculated from this profile correspond to a mean square roughness of $R_q = 0.55$ μm and a fractal Hurst exponent of $H = 0.76$.

averaged height-height correlation function $(g(r) = (H(x' + r) - H(x'))^2)$ can be computed. This allows the calculation of the root mean square roughness ($R_q = 0.55$ μm) and the Hurst exponent of the fractal surface structure ($H = 0.76$) (details are shown in fig. S2). Because of the small value of the surface roughness, our unheated superhydrophobic surface only traps small air pockets and therefore appears dark on the right rotor in Fig. 2B. Measurements of the torque-speed relationship show that, without active heating, the small value of the surface roughness leads to negligible drag reduction in comparison to a smooth, nonsuperhydrophobic rotor.

Although towing tanks, flow channels, and transient free-fall experiments have been used in previous studies (9, 16), to access turbulent flows and high Re's and to extract the skin friction component of the total drag, a bespoke wide-gap Taylor-Couette cell was used in this study. The advantages of using the Taylor-Couette cell for studying multiphase turbulent flows and for investigating the interaction of turbulence with superhydrophobic walls have recently been reviewed by Grossmann et al. (39). The torque transducer of a controlled stress rheometer (TA Instruments AR-G2) was used to measure the torque with high accuracy (as low as ±0.01 μN·m) while imposing a fixed angular velocity upon the submerged rotor. We calibrated the torque sensor by using well-characterized Newtonian fluids (the calibration oils were from Cannon Instrument Company), and the accuracy that can be attained is ±5%. Comparing the torque required to rotate a superhydrophobic rotor undergoing film boiling by active heating (Γ_{active}) to the torque for maintaining the same superhydrophobic rotor at the same angular velocity without active heating ($\Gamma_{passive}$) allows for direct determination of the skin friction drag reduction

$$\text{Skin friction reduction} = \frac{\Gamma_{passive} - \Gamma_{active}}{\Gamma_{passive}} \quad (1)$$

The Taylor-Couette rotor must be continuously heated during operation to maintain the film boiling state. Common technologies, such as inductive heating and slip rings, lead to unacceptable levels of noise in the torque acting on the rotor. To reduce these fluctuations, we designed a novel liquid metal interconnect that enables electrical power input to be delivered to an embedded resistive heater within the rotor. As illustrated in Fig. 3 (A and B), a cylindrical heater element was embedded along the rotation axis of the rotor, with power transmitted to it from a variable ac transformer via liquid metal contact. A eutectic alloy of gallium, indium, and tin (68.5%/21.5%/10% by weight; GalliumSource) was chosen as the liquid metal because of its low viscosity (0.0024 Pa · s), low melting point (−19°C), and high electrical conductivity (3.46×10^6 S/m) (40). Therefore, the only additional torque exerted on the rotor during heating was the frictional drag exerted by the low-viscosity liquid metal on the two moving contact wires. The resulting torque signal is measured to be 1050 μN·m, with a small SD of ±6.2 μN·m, as indicated by the black dashed lines in Fig. 4.

As illustrated in Fig. 3B, the submerged bottom face of the rotor was machined with a recess to trap an air bubble when submerged, serving to reduce additional end effects under rotation (*41*). The rotor was preheated to 160°C in air before submerging it into the water-filled Taylor-Couette cell. We built our Taylor-Couette flow cell to be mounted on a high-resolution controlled torque rheometer (TA Instruments AR-G2). The custom-designed rotor is mounted on the rheometer shaft through a plastic coupling that is precision-machined from a Torlon PAI (polyamide-imide; Solvay) ground rod. This plastic piece has a maximum operation temperature of about 260°C. Running at high electrical power results in the damage of this plastic connector and the loss of concentricity. To reduce the power input required to sustain film boiling, the water in the cell was also preheated to 86°C. Film boiling was established as soon as the preheated cylindrical rotor was immersed in the fluid,

and the rotor was then accelerated to a specified angular velocity. A sample trace of the measured torque as a function of time for a representative experiment is presented in Fig. 4. For the first 5 min, 40 W of power was continuously supplied through the liquid metal connector to the resistive heater embedded in the rotor. The torque required to maintain constant angular velocity was measured during this time. In Fig. 4, the angular velocity tested was 60 rad/s, which corresponds to $Re = 52,200$ in our system. Subsequently, the power to the heater was turned off. The continuous vapor film, with no power input to sustain it, gradually collapses over the following 50 s, and the surface transitions to the nucleate boiling condition. The torque required to maintain the same angular velocity gradually increased over the transition time. During the entire experiment, the water temperature was found to rise slightly to 91°C. The liquid metal exerts a torque
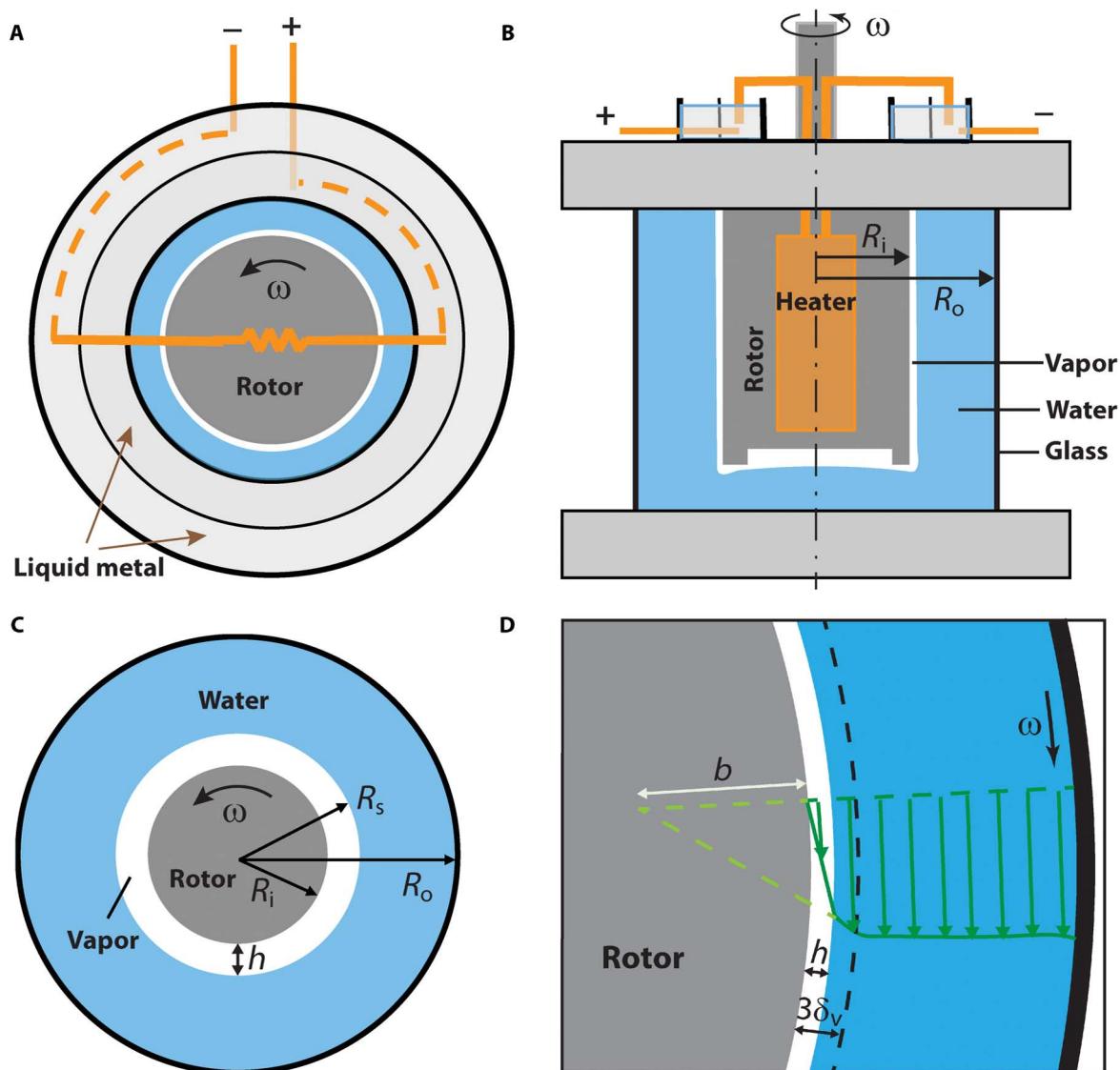

Fig. 3. Schematic illustrations of the Taylor-Couette cell setup and velocity profile in the cell. (**A**) Top view showing the electrical connection from the external power source through liquid metal channels, with the heater represented as a resistor. (**B**) Front view of the full setup showing the heater embedded in the rotor and the liquid metal channels mounted upon the Taylor-Couette cell. (**C**) A schematic illustration showing a rotating inner rotor of radius R_i operating above the Leidenfrost temperature T_L, generating a vapor film of thickness h in a cell of radius R_o. (**D**) Turbulent fluid velocity profile in the Taylor-Couette cell showing slip boundary condition at the interface of the water and the inner rotor due to the existence of the vapor film. In the reference frame of the steadily rotating inner rotor, the outer wall now appears to be rotating clockwise with an angular velocity ω.

contribution upon the contact wires, which can be directly calibrated in each experiment. Subtracting the liquid metal torque contribution from the total measured torque determines the values of Γ_{active} and $\Gamma_{passive}$. Comparing the values of these two torques using Eq. 1 then allows for the calculation of the skin friction drag reduction. At a rotation rate of 60 rad/s, the drag reduction relative to the superhydrophobic rotor without heating was measured to be 82 ± 12%, considerably higher than values previously achieved on a spray-coated superhydrophobic surface at ambient temperature with respect to a flat nonsuperhydrophobic surface (7). We have also performed additional experiments in which we switch the heater off, allowing the vapor film to collapse, and then switch the heater back on. As shown in fig. S3, the same level of drag reduction (within measurement uncertainty) can be reestablished by restoring a Leidenfrost vapor film, indicating that the drag reduction effect can be switched on and off as needed. However, we do notice that long time exposure to nucleation boiling in water can render the superhydrophobic aluminum surface hydrophilic, which is most likely due to boehmitization of the surface (38). Other low-temperature Leidenfrost surfaces with enhanced stability to the large thermomechanical stresses resulting from nucleate boiling can potentially solve this problem in practical applications (32).

This large skin friction drag reduction can be rationalized using an appropriate two-fluid layer theory. For simplicity, we work in a steadily rotating reference frame, and we consider a system with a stationary inner cylinder of radius R_i = 14 mm surrounded by a layer of steam of uniform thickness h in a water-filled cylinder of outer radius R_o = 34 mm steadily rotating at an angular velocity of Ω (Fig. 3, B and C). The wetted height of the rotor in contact with water is L = 40 mm. We make use of the skin friction law derived by Srinivasan et al. (7) for turbulent flow adjacent to a superhydrophobic surface in a Taylor-Couette cell system, which posits that the dimensionless velocity in the viscous sublayer of the turbulent flow is shifted by a constant value, b^+, that is given by the expression

$$\frac{V_i}{u_\tau} = M \ln Re_\tau + N + b^+ \qquad (2)$$

Equation 2 has also been validated using numerical simulations of turbulent shear flows near walls with a Navier slip boundary condition
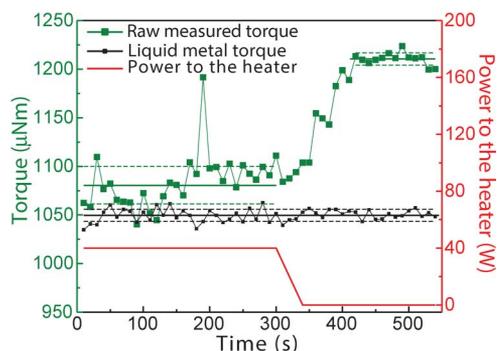
Fig. 4. Measured torque (green) for a single experiment (at an angular velocity of ω = 60 rad/s, corresponding to Re = 52,200) showing drag reduction by establishing a Leidenfrost vapor film. As indicated by the red curve, power is supplied to the embedded heater for the first 300 s, resulting in a lower measured torque with active heating. When the electrical heating is turned off, the frictional torque steadily increases. To calculate the percent drag reduction arising from the Leidenfrost effect, the torque exerted by the liquid metal on the contact wires (as indicated by the black curve) must be subtracted from the measured torque.

(42, 43). Here, $V_i = \Omega R_i$ represents the velocity of the inner rotor, $u_\tau = \sqrt{\tau_i/\rho_l}$ is the friction velocity, where $\tau_i = \Gamma_i/(2\pi R_i^2 L)$ is the local wall shear stress acting on the rotor, Γ_i is the torque measured on the inner rotor, and ρ_l is the liquid density. $Re_\tau = u_\tau(R_o - R_i)/\nu_l$ is the friction Re (where $\nu_l = \mu_l/\rho_l$ is the kinematic viscosity of the liquid). The first two terms on the right-hand side of Eq. 2 pertain to an untreated, smooth, no-slip surface. M and N are geometry-dependent constants and are determined by fitting torque-speed data obtained with an untreated (nonsuperhydrophobic) and unheated rotor. Here, we use the unheated superhydrophobic rotor because the very small surface roughness leads to negligible drag reduction with respect to a smooth rotor. For this system, we find M = 3.8 ± 0.1 and N = − 12.5 ± 0.1. The presence of a local slip boundary condition on a heated superhydrophobic surface gives rise to the final term in Eq. 2. Here, b^+ is the dimensionless slip length expressed in wall units $b^+ = b/\delta_v$, where δ_v is the viscous length $\delta_v = \nu_l/u_\tau$. As illustrated in Fig. 3D, the slip length b physically represents the distance into the wall that the velocity profile must be extrapolated to give a nonslip condition at the wall (44). For the Taylor-Couette cell geometry, we have shown previously (7) that this dimensionless slip length can be written in the form

$$b^+ = \frac{b}{\delta_v} = \left(\frac{b}{R_o - R_i}\right) Re \sqrt{\frac{C_f}{2}} \qquad (3)$$

where $C_f = \tau_i/\left(\frac{1}{2}\rho V_i^2\right) = 2(u_\tau/V_i)^2$ is the coefficient of skin friction and $Re = V_i(R_o - R_i)/\nu_l$ is the wall Re. For an experiment performed at a controlled rotation rate $V_i = \Omega R_i$ and a measured torque Γ_i, the product $Re\sqrt{C_f/2}$ is identical to the friction Re ($Re_\tau = u_\tau(R_o - R_i)/\nu_l$), which is directly determined in the Taylor-Couette experiment.

We maintain the inner rotor at the same rotation speed (V_i) with or without active heating. Thus, the skin friction reduction is reflected by the change in the coefficient of skin friction, and Eq. 1 can now be rewritten as

$$\text{Skin friction reduction} = \frac{\Gamma_{passive} - \Gamma_{active}}{\Gamma_{passive}}$$
$$= \frac{C_{f,passive} - C_{f,active}}{C_{f,passive}} \qquad (4)$$

Combining Eq. 3 with Eq. 2 gives rise to the final expression

$$\sqrt{\frac{2}{C_f}} = M \ln\left(Re\sqrt{\frac{C_f}{2}}\right) + N + \left(\frac{b}{R_o - R_i}\right) Re\sqrt{\frac{C_f}{2}} \qquad (5)$$

Here, V_i/u_τ and Re_τ are represented by the quantities $\sqrt{2/C_f}$ and $Re\sqrt{C_f/2}$, respectively. Drag reduction data were obtained for Re's in the range 26,100 ≤ Re ≤ 52,000, and the results are plotted in Fig. 5, along with a fit for the slip length obtained using Eq. 5. The agreement between theory and the experimental data is excellent. The vertical blue dashed line indicates the critical Re, $Re_c = 1.2 \times 10^4$, beyond which the flow in this wide-gap Taylor-Couette cell can be considered to be fully turbulent (7). Drag reduction in turbulent flow on a passive superhydrophobic surface is small at low Re's and increases to a maximum of 22% at Re = 80,000 (7), whereas the turbulent drag reduction on our low-temperature Leidenfrost surface approaches 80 to 90% at much lower Re's. The regression of Eq. 5 (the black curve in Fig. 5), with the single

unknown parameter being the slip length, corresponds to a slip length of $b = 1.04 \pm 0.26$ mm, which is two orders of magnitude larger than that measured for a passive superhydrophobic surface (7). The larger slip length arises from two complementary factors: First, the vapor layer is continuous, leading to a complete slip boundary condition around the rotor (rather than a partially wetted Cassie-Baxter state); second, as we show below, the vapor layer is much thicker than the local air layer trapped by a typical superhydrophobic surface.

We calculate the thickness of the vapor layer by relating it to the slip length b. Although the bulk flow is turbulent in nature ($Re > Re_c = 1.2 \times 10^4$), the flow in the region of interest (close to the wall, in the viscous sublayer) is dominated by viscous interactions. Moreover, very close to the wall, the Reynolds stresses in the flow can be neglected, leading to a mean velocity profile that is linear (45). This region is known as the linear sublayer and extends out from the wall to at least $y^+ \simeq 3$, where $y^+ = y/\delta_v$ represents nondimensional wall units. Here, y is the physical distance from the wall, and δ_v is the viscous length scale. For the flows considered in this study ($Re = [26,100, 52,200]$), the viscous length scale is calculated to be $\delta_v = [32.7, 22.3]$ μm. Therefore, the linear sublayer region has a thickness in the range of $3\delta_v = [98.1, 66.9]$ μm. These considerations allow us to adopt a laminar model to estimate the slip length. Because the thickness of the linear sublayer ($3\delta_v$) is two orders of magnitude smaller than the rotor radius (R_i) (Fig. 3D) and the Taylor-Couette flow is axisymmetric, we use the slip length for steady shearing flow between two parallel plates, derived previously by Vinogradova (46) and McHale et al. (18), for a low-viscosity lubricating layer adjacent to the wall. The resulting slip length and the thickness of the lubricating vapor layer are related by the expression

$$\frac{b}{h} = \left[\frac{\mu_l}{\mu_v}\right] - 1 \tag{6}$$

Thus, the slip length scales with the thickness of the vapor film h, augmented by the viscosity ratio of the two fluids μ_l/μ_v. A high viscosity ratio between the skewed liquid water and the local water vapor layer adjacent to the wall is essential to achieving a large slip length and therefore a high level of drag reduction.
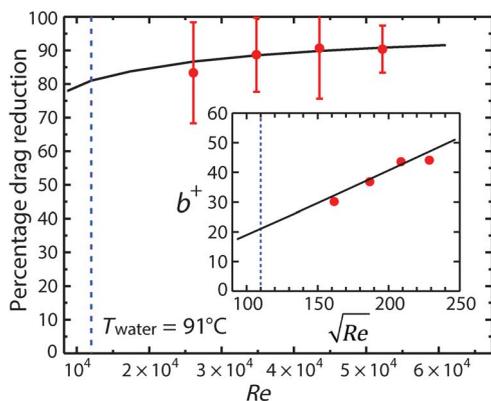
Fig. 5. Skin friction reduction in a turbulent Taylor-Couette flow resulting from the low-temperature Leidenfrost effect. Fitting the experimental results (represented by red dots) using Eq. 5 gives a slip length of $b = 1.04$ mm (indicated by the black curve). The dashed blue line marks the transition to turbulent flow at $Re = 12,000$. The evolution in dimensionless slip length b^+ with $\sqrt{Re}$ is shown in the inset plot, indicating excellent agreement between experiment and theory.

Given that the viscosity ratio for water (at $T_w = 91°C$) and its saturated vapor is approximately $\mu_l/\mu_v = 25$ (47) and that the fitted slip length is $b = 1.04 \pm 0.26$ mm, Eq. 6 can be used to calculate the expected thickness of the vapor film to be $h = 44 \pm 11$ μm, in agreement with the range of experimentally measured values for a Leidenfrost film (48, 49). Knowing the geometry of the rotor and the Taylor-Couette flow cell, we can estimate the vapor volume fraction to be on the order of 10^{-3}. Using this value for the vapor film thickness, the expected locus of the vapor-water boundary lies within the viscous sublayer, and the laminar assumption is valid. We note that, in the above calculation, we assume that the vapor film that encompasses the rotor surface has a uniform axial thickness, although, in practice, because of natural convection, the thickness of the vapor film will also vary along the axial length of the rotor. Assuming a stable laminar vapor film with a smooth vapor-liquid interface, previous studies have analytically addressed film boiling heat transfer in a manner similar to that for laminar film condensation (50–52). For film boiling on a vertical surface with a length scale of a few centimeters, the analytical results agree well with experimental data (53). In our experimental setup, the vertical surface has an axial length of $L = 40$ mm. This allows us to model the film boiling using the laminar film vapor flow approach, and the maximum thickness h_{max} of the vapor film is calculated to be

$$h_{max} = \left(\frac{4\mu_v k_v L(T_w - T_{sat})}{\rho_v(\rho_l - \rho_v)gH_{lv}}\right)^{\frac{1}{4}} = 88 \text{ μm} \tag{7}$$

where $\mu_v = 1.2 \times 10^{-5}$ Pa·s and $k_v = 0.016$ W/(m·K) are the viscosity and thermal conductivity of the saturated water vapor, respectively. $T_w - T_{sat} = 25$ K is the wall superheat, $\rho_v = 0.59$ kg/m³ is the density of the saturated water vapor, $\rho_l = 9.65 \times 10^2$ kg/m³ is the density of water at 91°C, $g = 9.8$ m/s² is the gravitational acceleration, and $H_{lv} = 2.265 \times 10^6$ J/kg is the latent heat of vaporization. This simple model of course neglects the additional effects of centrifugal forces caused by the rotation, as well as possible vortices and bubbles that are generated in vapor film boiling (53, 54), all of which cause additional fluctuations in the instantaneous film thickness profile. Nevertheless, the estimated vapor film thickness determined in our experiments is in agreement with the analytically calculated vapor film thickness. We note that, in our experiment, the vapor film volume (thickness) has a weaker dependence on the axial length ($h \sim L^{1/4}$), in comparison with the gas concentration dependence on the axial length in bubbly turbulent Taylor-Couette flows (55). This difference arises from the distribution of the gas phase. In our experiment, the vapor phase is located as a continuous film almost entirely adjacent to the liquid-solid interface, rather than distributed throughout the Couette cell as expected in a bubbly turbulent flow. The vapor film completely envelops the rotor, forming an annular channel at the liquid-solid interface through which vapor can vent and escape.

Our results show that substantial friction reduction can be obtained at a steady state, provided that power is actively supplied to sustain the boiling film and prevent the collapse of the Leidenfrost state. We have demonstrated that using a textured superhydrophobic surface can substantially reduce the required power input. For large waterborne vehicles, this thermal energy would, in principle, be supplied by the waste heat generated from vehicle engines. In the current experimental setup, the energy efficiency, estimated by calculating how much power is saved in skin friction reduction (($T_{passive} - T_{active}$)ω) as a fraction of the electric power $\hat{W}$ inputted to sustain the boiling film ($\hat{W} = 40$ W), is less than 1%

$((T_{passive} - T_{active})\omega/\hat{W} < 1\ \%)$. For certain military applications, such as torpedoes, where energy efficiency is a secondary consideration to gains in vehicle speed, the high-percentage skin friction reduction of our current approach offers major advantages. Further, this technology only requires the delivery of heat to the hull surface. Therefore, it is possible to use it as a complementary technology to other drag reduction methods on water vehicles, such as microbubble injection or polymer drag reduction (4, 8).

CONCLUSIONS

In summary, we have demonstrated skin friction reduction in excess of 90% in turbulent Taylor-Couette flows at $Re = 52{,}200$. The creation of a low-temperature Leidenfrost state with a continuous and thick vapor film in between the rotor and the water leads to an apparent slip layer and reduction in the average shear stress acting on the rotor, which can be quantitatively described by a slip boundary layer theory. The large thickness of the vapor film, amplified by a factor that depends on the ratio of the liquid and vapor viscosities, results in a slip length of $b \simeq 1$ mm, which is two orders of magnitude larger than that achieved by a passive superhydrophobic surface in the same test geometry (7). The microtextured superhydrophobic surface we have developed reduces the wall superheat conditions that are required to less than $T_w - T_{sat} \leq 25$ K and greatly reduces the heat flux that must be delivered to sustain the plastron film. Turbulent fluctuations at high Re can lead to degradation in the levels of friction reduction, but the constant generation of steam in the boiling film allows for replenishing of the continuous vapor layer, and this leads to sustained drag reduction.

MATERIALS AND METHODS
Fabrication of the Taylor-Couette rotor
The Taylor-Couette rotor was machined manually from a solid 6061 aluminum cylinder. As shown in fig. S1, the rotor has a diameter of 28 mm with a surface finish of 8G in the lower section. The top section features notched radii: The larger one allows for boiling steam to vent from the Taylor-Couette cell, and the smaller one enables interfacing with the stem of the rotor. A recess was bored into the lower axial face of the rotor to trap a bubble of air when the rotor was submerged and to reduce additional frictional end effects under rotation. An additional recess was bored into the top face of the rotor, into which the cartridge heater (McMaster-Carr, model 3618K352, with a stainless steel sheath and a maximum power rating of 250 W) was inserted. The wire leads of the heater were cut, resoldered with an 18-gauge magnet wire, and passed into the rotor's stem.

To prevent the leakage of thermal energy from the heated rotor into the body of the rheometer, Torlon PAI (Solvay) was selected as the appropriate material for fabricating a thermally insulated stem that connects the rotor to the rheometer. The stem was turned and bored manually using a carbide tool to a surface finish of 16G and fabricated with holes at both ends that interfaced with the motor shaft of the rheometer on top and with the aluminum rotor at the bottom. Radial holes drilled through the stem allowed the leads of the heater to pass through and dip into the liquid metal channels.

Preparation and characterization of the superhydrophobic surface
The fabricated rotor was immersed in a beaker containing 70-ml 18 wt% hydrochloride solution for 90 s to introduce random microscale surface roughness through an etching process. This was followed by immediate withdrawal from the etching solution, washing with excess deionized water, and then sonication in clean water for 30 min. Before coating with a fluorosilane hydrophobizing agent, the rotor was washed with acetone to remove any residual oil contamination from the machining process. After sonication, the rotor was dried in an air stream at room temperature before thermal treatment at 600°C for 24 hours to induce a passivation layer on the metal. The textured and passivated metal was rendered superhydrophobic by immersing in a solution of perfluorooctyltriethoxysilane in hexane (7 μl/ml) for 24 hours, followed by baking in an oven at 120°C for 1 hour to ensure the chemical bonding of silane molecules to the surface.

To characterize the superhydrophobic surface created through this process, a flat 6061 aluminum coupon was treated in the same way and was characterized using scanning electron microscopy (JEOL 6010LA) and atomic force microscopy (Veeco Nanoscope V with Dimension 3100, D31005-1) in the tapping mode using a silicon probe (Bruker, MPP-11100-10). The contact angle measurements and the lifetime of a drop experiment were conducted with a goniometer (ramé-hart, model 590).

Fabrication of the Taylor-Couette cell
The wide-gap Taylor-Couette cell was fabricated in the Edgerton Student Shop at the Massachusetts Institute of Technology. Two plates of 6061 aluminum were turned manually to a diameter of 149.9 mm and thicknesses of 10.2 and 22.9 mm, with a surface finish of 8G. Blind holes were bored on each side of the thicker plate. The first of these holes (diameter, 106.1 mm; depth, 7.6 mm) was used to connect to the Peltier plate of the AR-G2 rheometer via a tight sliding fit, whereas the second (diameter, 74.9 mm; depth, 6 mm) included an undercut that housed an O-ring. An identical blind hole with a seal was also bored into the thinner aluminum plate, and a glass cylinder was housed between the two plates by inserting each end into the sealed blind hole of one of the plates. Finally, a through-hole was bored into the thinner plate, with a diameter 2 mm larger than that of the Taylor-Couette rotor, such that it could be inserted and retracted vertically from the cell.

Fabrication of the liquid-metal contact setup
The liquid metal used was a eutectic alloy of gallium, indium, and tin, with a ratio of Ga 68.5%/In 21.5%/Sn 10% by weight. The liquid metal holder was fabricated by milling U-shaped channels into a single plate of polycarbonate using a computer numerical control machine with high-speed steel tooling. A surface finish of 16G was achieved. When not in use, the eutectic was stored under 1 M HCl to prevent oxidation by air.

Setup and experimental procedure
The Taylor-Couette cell was mounted to the Peltier plate of a TA Instruments AR-G2 rheometer and filled with preheated deionized water. The Peltier plate was used to preheat the water temperature to 86°C. The polycarbonate holder with concentric channels containing liquid metal was placed on top of the cell. The superhydrophobic rotor was then attached to the rheometer via its plastic stem. Before the rotor was submerged in water, a variable autotransformer (Variac) was connected directly to the leads of the heater, and the rotor was heated to 160°C in air. The autotransformer was then disconnected from the heater, and the hot rotor was plunged into the Taylor-Couette cell, resulting in immediate film boiling on the surface of the rotor. The leads of the heater were then submerged in the liquid metal, and the autotransformer

was connected to send power (40 W) to the heater cartridge through the liquid metal connector. In the sample test shown in Fig. 4, the speed of the rotor was increased to 60 rad/s over 1 min and maintained throughout the experiment. After 5 min, the power supplied by the autotransformer was gradually decreased to zero to avoid transient current spikes. The experiment then continued for another 10 min while the thermal energy in the rotor was transferred into the viscous liquid and dissipated until the film boiling was lost. The torque required to maintain the rotor at the same speed was recorded over the entire heated and unheated periods. To measure the torque that the liquid metal exerted on the moving wire leads, we deducted the total torque measured when the rotor was maintained at the same speed, without active heating, and not in contact with liquid metal from the total torque measured when the rotor was running under the same condition but with the leads in contact with liquid metal.

SUPPLEMENTARY MATERIALS

Supplementary material for this article is available at http://advances.sciencemag.org/cgi/content/full/2/10/e1600686/DC1

fig. S1. Geometry of the Taylor-Couette rotor used in the present friction drag reduction experiments.

fig. S2. Hurst exponent plot for the chemically treated and textured surface.

fig. S3. Restoration of a low-temperature Leidenfrost film and drag-reducing state upon first ceasing, and then restoring, electrical heating of the Taylor-Couette rotor at $Re = 52,200$.

REFERENCES AND NOTES

1. D. W. Bechert, M. Bruse, W. Hage, J. G. T. Van der Hoeven, G. Hoppe, Experiments on drag-reducing surfaces and their optimization with an adjustable geometry. *J. Fluid Mech.* **338**, 59–87 (1997).
2. B. Dean, B. Bhushan, Shark-skin surfaces for fluid-drag reduction in turbulent flow: A review. *Philos. Trans. R. Soc. London Ser. A* **368**, 4775–4806 (2010).
3. A. White, Drag of spheres in dilute high polymer solutions. *Nature* **216**, 994–995 (1967).
4. C. M. White, M. G. Mungal, Mechanics and prediction of turbulent drag reduction with polymer additives. *Annu. Rev. Fluid Mech.* **40**, 235–256 (2008).
5. B. R. Solomon, K. S. Khalil, K. K. Varanasi, Drag reduction using lubricant-impregnated surfaces in viscous laminar flow. *Langmuir* **30**, 10970–10976 (2014).
6. C. Schönecker, T. Baier, S. Hardt, Influence of the enclosed fluid on the flow over a microstructured surface in the Cassie state. *J. Fluid Mech.* **740**, 168–195 (2014).
7. S. Srinivasan, J. A. Kleingartner, J. B. Gilbert, R. E. Cohen, A. J. B. Milne, G. H. McKinley, Sustainable drag reduction in turbulent Taylor-Couette flows by depositing sprayable superhydrophobic surfaces. *Phys. Rev. Lett.* **114**, 014501 (2015).
8. S. L. Ceccio, Friction drag reduction of external flows with bubble and gas injection. *Annu. Rev. Fluid Mech.* **42**, 183–203 (2010).
9. I. U. Vakarelski, J. O. Marston, D. Y. C. Chan, S. T. Thoroddsen, Drag reduction by Leidenfrost vapor layers. *Phys. Rev. Lett.* **106**, 214501 (2011).
10. A. Busse, N. D. Sandham, G. McHale, M. I. Newton, Change in drag, apparent slip and optimum air layer thickness for laminar flow over an idealised superhydrophobic surface. *J. Fluid Mech.* **727**, 488–508 (2013).
11. M. N. Kavalenka, F. Vüllers, S. Lischker, C. Zeiger, A. Hopf, M. Röhrig, B. E. Rapp, M. Worgull, H. Hölscher, Bioinspired air-retaining nanofur for drag reduction. *ACS Appl. Mater. Interfaces* **7**, 10651–10655 (2015).
12. J. P. Rothstein, Slip on superhydrophobic surfaces. *Annu. Rev. Fluid Mech.* **42**, 89–109 (2010).
13. B. J. Rosenberg, T. Van Buren, M. K. Fu, A. J. Smits, Turbulent drag reduction over air- and liquid-impregnated surfaces. *Phys. Fluids* **28**, 015103 (2016).
14. I. U. Vakarelski, D. Y. C. Chan, S. T. Thoroddsen, Drag moderation by the melting of an ice surface in contact with water. *Phys. Rev. Lett.* **115**, 044501 (2015).
15. K. Fukuda, J. Tokunaga, T. Nobunaga, T. Nakatani, T. Iwasaki, Y. Kunitake, Frictional drag reduction with air lubricant over a super-water-repellent surface. *J. Mar. Sci. Technol.* **5**, 123–130 (2000).
16. I. U. Vakarelski, D. Y. C. Chan, S. T. Thoroddsen, Leidenfrost vapour layer moderation of the drag crisis and trajectories of superhydrophobic and hydrophilic spheres falling in water. *Soft Matter* **10**, 5662–5668 (2014).
17. N. J. Shirtcliffe, G. McHale, M. I. Newton, Y. Zhang, Superhydrophobic copper tubes with possible flow enhancement and drag reduction. *ACS Appl. Mater. Interfaces* **1**, 1316–1323 (2009).
18. G. McHale, M. I. Newton, N. J. Shirtcliffe, Immersed superhydrophobic surfaces: Gas exchange, slip and drag reduction properties. *Soft Matter* **6**, 714–719 (2010).
19. C. Ybert, C. Barentin, C. Cottin-Bizonne, P. Joseph, L. Bocquet, Achieving large slip with superhydrophobic surfaces: Scaling laws for generic geometries. *Phys. Fluids* **19**, 123601 (2007).
20. R. J. Daniello, N. E. Waterhouse, J. P. Rothstein, Drag reduction in turbulent flows over superhydrophobic surfaces. *Phys. Fluids* **21**, 085103 (2009).
21. C.-H. Choi, C.-J. Kim, Large slip of aqueous liquid flow over a nanoengineered superhydrophobic surface. *Phys. Rev. Lett.* **96**, 066001 (2006).
22. L. Bocquet, E. Lauga, A smooth future? *Nat. Mater.* **10**, 334–337 (2011).
23. M. Xu, G. Sun, C.-J. Kim, Infinite lifetime of underwater superhydrophobic states. *Phys. Rev. Lett.* **113**, 136103 (2014).
24. P. Lv, Y. Xue, Y. Shi, H. Lin, H. Duan, Metastable states and wetting transition of submerged superhydrophobic structures. *Phys. Rev. Lett.* **112**, 196101 (2014).
25. R. Poetes, K. Holtzmann, K. Franze, U. Steiner, Metastable underwater superhydrophobicity. *Phys. Rev. Lett.* **105**, 166104 (2010).
26. S. Srinivasan, S. S. Chhatre, J. O. Guardado, K.-C. Park, A. R. Parker, M. F. Rubner, G. H. McKinley, R. E. Cohen, Quantification of feather structure, wettability and resistance to liquid penetration. *J. R. Soc. Interface* **11**, 20140287 (2014).
27. C. Lee, C.-J. Kim, Underwater restoration and retention of gases on superhydrophobic surfaces for drag reduction. *Phys. Rev. Lett.* **106**, 014502 (2011).
28. H. Schmid, Less emissions through waste heat recovery, in *Green Ship Technology Conference*, London, U.K., 28–29 April 2004.
29. T. L. Bergman, F. P. Incropera, A. S. Lavine, *Fundamentals of Heat and Mass Transfer* (John Wiley & Sons, 2011).
30. J. G. Leidenfrost, *De Aquae Communis Nonnullis Qualitatibus Tractatus* (Ovenius, 1756).
31. D. Quéré, Leidenfrost dynamics. *Annu. Rev. Fluid Mech.* **45**, 197–215 (2013).
32. H. O'Hanley, C. Coyle, J. Buongiorno, T. McKrell, L.-W. Hu, M. Rubner, R. Cohen, Separate effects of surface roughness, wettability, and porosity on the boiling critical heat flux. *Appl. Phys. Lett.* **103**, 024102 (2013).
33. I. U. Vakarelski, N. A. Patankar, J. O. Marston, D. Y. C. Chan, S. T. Thoroddsen, Stabilization of Leidenfrost vapour layer by textured superhydrophobic surfaces. *Nature* **489**, 274–277 (2012).
34. L.-W. Fan, J.-Q. Li, D.-Y. Li, L. Zhang, Z.-T. Yu, Regulated transient pool boiling of water during quenching on nanostructured surfaces with modified wettability from superhydrophilic to superhydrophobic. *Int. J. Heat Mass Transfer* **76**, 81–89 (2014).
35. J. D. Bernardin, I. Mudawar, The Leidenfrost point: Experimental study and assessment of existing models. *J. Heat Transfer* **121**, 894–903 (1999).
36. A. B. D. Cassie, S. Baxter, Wettability of porous surfaces. *Trans. Faraday Soc.* **40**, 546–551 (1944).
37. G. Dupeux, P. Bourrianne, Q. Magdelaine, C. Clanet, D. Quéré, Propulsion on a superhydrophobic ratchet. *Sci. Rep.* **4**, 5280 (2014).
38. P. Kim, M. J. Kreder, J. Alvarenga, J. Aizenberg, Hierarchical or not? Effect of the length scale and hierarchy of the surface roughness on omniphobicity of lubricant-infused substrates. *Nano Lett.* **13**, 1793–1799 (2013).
39. S. Grossmann, D. Lohse, C. Sun, High–Reynolds number Taylor-Couette turbulence. *Annu. Rev. Fluid Mech.* **48**, 53–80 (2016).
40. P. Surmann, H. Zeyat, Voltammetric analysis using a self-renewable non-mercury electrode. *Anal. Bioanal. Chem.* **383**, 1009–1013 (2005).
41. L. Bocquet, P. Tabeling, S. Manneville, Comment on "Large slip of aqueous liquid flow over a nanoengineered superhydrophobic surface". *Phys. Rev. Lett.* **97**, 109601 (2006).
42. T. Min, J. Kim, Effects of hydrophobic surface on skin-friction drag. *Phys. Fluids* **16**, L55–L58 (2004).
43. H. Park, H. Park, J. Kim, A numerical study of the effects of superhydrophobic surface on skin-friction drag in turbulent channel flow. *Phys. Fluids* **25**, 110815 (2013).
44. E. Lauga, M. Brenner, H. Stone, in *Springer Handbook of Experimental Fluid Mechanics* (Springer, 2007), pp. 1219–1240.
45. M. Wosnik, L. Castillo, W. K. George, A theory for turbulent pipe and channel flows. *J. Fluid Mech.* **421**, 115–145 (2000).
46. O. I. Vinogradova, Drainage of a thin liquid film confined between hydrophobic surfaces. *Langmuir* **11**, 2213–2220 (1995).
47. A. Nagashima, Viscosity of water substance—New international formulation and its background. *J. Phys. Chem. Ref. Data* **6**, 1133–1166 (1977).
48. A.-L. Biance, C. Clanet, D. Quéré, Leidenfrost drops. *Phys. Fluids* **15**, 1632 (2003).
49. F. Bonsignore, thesis, Rochester Institute of Technology (1981).
50. L. A. Bromley, Heat transfer in stable film boiling. *Chem. Eng. Progr.* **46**, 221–227 (1950).
51. R. Cess, Analysis of laminar film boiling from a vertical flat plate, in *Research Report 405 FF 340-R2-X* (Westinghouse Research Lab, 1959).
52. J. Koh, Analysis of film boiling on vertical surfaces. *J. Heat Transfer* **84**, 55–62 (1962).
53. T. D. Bui, V. K. Dhir, Film boiling heat transfer on an isothermal vertical surface. *J. Heat Transfer* **107**, 764–771 (1985).

54. S. G. Huisman, R. C. A. van der Veen, C. Sun, D. Lohse, Multiple states in highly turbulent Taylor–Couette flow. *Nat. Commun.* **5**, 3820 (2014).

55. D. P. M. van Gils, D. N. Guzman, C. Sun, D. Lohse, The importance of bubble deformability for strong drag reduction in bubbly turbulent Taylor–Couette flow. *J. Fluid Mech.* **722**, 317–347 (2013).

Citation: D. Saranadhi, D. Chen, J. A. Kleingartner, S. Srinivasan, R. E. Cohen, G. H. McKinley, Sustained drag reduction in a turbulent flow using a low-temperature Leidenfrost surface. *Sci. Adv.* **2**, e1600686 (2016).

Science Advances

Sustained drag reduction in a turbulent flow using a low-temperature Leidenfrost surface

Dhananjai Saranadhi, Dayong Chen, Justin A. Kleingartner, Siddarth Srinivasan, Robert E. Cohen and Gareth H. McKinley

ARTICLE TOOLS	http://advances.sciencemag.org/content/2/10/e1600686
SUPPLEMENTARY MATERIALS	http://advances.sciencemag.org/content/suppl/2016/10/11/2.10.e1600686.DC1
REFERENCES	This article cites 49 articles, 0 of which you can access for free http://advances.sciencemag.org/content/2/10/e1600686#BIBL
PERMISSIONS	http://www.sciencemag.org/help/reprints-and-permissions

Use of this article is subject to the Terms of Service